Submitted to Scanning Electron Microscopy/1984

CONF-840413--2

BNL-35338

# SYNCHROTRON X-RAY FLUORESCENCE AND EXTENDED X-RAY ABSORPTION FINE STRUCTURE ANALYSIS

J.R. Chen*[1], B.M. Gordon[2], A.L. Hanson[2], K.W. Jones[2], H.W. Kraner[2], E.C.T. Chao[3], and J.A. Minkin[3]

[1]State University of New York at Geneseo, Geneseo, NY; [2]Brookhaven National Laboratory, Upton, NY; [3]U.S. Geological Survey, Reston, VA

BNL--35338

DE85 003606

## Abstract

The advent of dedicated synchrotron radiation sources has led to a significant increase in activity in many areas of science dealing with the interaction of x-rays with matter. Synchrotron radiation provides intense, linearly polarized, naturally collimated, continuously tunable photon beams, which are used to determine not only the elemental composition of a complex, polyatomic, dilute material but also the chemical form of the elements with improved accuracy. Examples of the application of synchrotron radiation include experiments in synchrotron x-ray fluorescence (SXRF) analysis and extended x-ray absorption fine structure (EXAFS) analysis. New synchrotron radiation x-ray microprobes for elemental analysis in the parts per billion range are under construction at several laboratories.

KEY WORDS: synchrotron radiation, x-ray fluorescence, extended x-ray absorption fine structure, particle induced x-ray emission, elemental analysis, trace element, minimum detectable limits, x-ray microprobe.

*Address for correspondence:

Physics Department
State University of New York
College at Geneseo
Geneseo, NY 14454 Phone No. (716) 245-5283

## Introduction

The advent of intense, linearly polarized, naturally collimated, continuously tunable photon beams from dedicated high energy storage rings has led to a significant increase in activity in many areas of science dealing with the interaction of x-rays with matter. As evidenced by the sharp increase in the number of publications and users of synchrotron radiation,[65] these areas include, for example, biology, chemistry, electrical engineering, condensed-matter physics, geology, materials science, medicine and surface science. The underlying theme that unifies the activity in these fields is synchrotron radiation's ability to determine not only the elemental composition of a complex polyatomic dilute material but also the chemical form of the elements with vastly improved accuracy. This new capability comes at a time when there is renewed interest in atomic level phenomena aimed at understanding, for example, the role of trace elements in a variety of geological materials, the functioning of biological structures on the microscopic scale, the replication of very large scale integrated (VLSI) circuits, the action of impurities in super-conductors, coal and other materials, the imperfection and growth of crystals, and the mechanisms involved in corrosion and catalysis.[2,73,44]

This paper presents a general introduction to what synchrotron radiation is and the properties that make it valuable. We focus attention on the x-ray region of the synchrotron radiation spectrum, which is less developed than the vacuum ultraviolet region, where extensive research and reviews already exist.[73,44,17,75] As examples of the application of x-ray synchrotron radiation we consider several noteworthy experiments using synchrotron x-ray fluorescence (SXRF) and extended x-ray absorption fine structure (EXAFS) analyses. In conclusion, the capabilities of the new x-ray microprobes for elemental analysis are discussed with an emphasis on some of the future uses of synchrotron radiation. Numerical parameters, when useful, are cited for the recently commissioned x-ray storage ring at the National Synchrotron Light Source (NSLS) at Brookhaven National Laboratory, New York.[70]

## Production of Synchrotron Radiation

### Radiation from an Accelerated Charge

Whenever electric charges are accelerated they emit electromagnetic radiation.[36] Examples of this phenomenon include the sinusoidal linear acceleration of electrons in an antenna which leads to radio waves, the scattering of electrons by the nucleus of an atom which produces bremsstrahlung, and the centripetal acceleration of (non-relativistic) relativistic electrons constrained to circular orbits by a magnetic field which produces (cyclotron) synchrotron radiation. The magnetic field could be that of the interstellar medium[22] or the bending magnet of an accelerator.

Cyclotron radiation occurs at a single frequency:

$$\omega_{cyclotron} = \frac{eB}{m} \qquad (1)$$

where e and m are the charge and mass of the electron, respectively, and B is the strength of the magnetic field. At any one instant in time, the spatial distribution of the radiation is given by the Poynting vector $|\vec{S}(\vec{r},t)|$ viz.,

$$|\vec{S}(\vec{r},t)| = \frac{e^2|\vec{a}(t')|^2 \sin^2\theta_L}{4\pi c^3 r^2} \qquad (2)$$

where $\vec{a}$ is the acceleration of the electron. See figure 1a. The radiated intensity is proportional to $\sin^2\theta_L$ and is maximum along the tangent to the orbit. The 3-dimensional doughnut shaped radiation pattern is shown in figure 1b. The total radiated power is obtained by integrating equation (2) and is given by the Larmor formula:

$$P = \frac{2e^2|\vec{a}(t')|^2}{3c^3} \qquad (3)$$

The polarization of the radiation is dependent on the direction of observation as shown in figure 2.

### Synchrotron Radiation

For relativistic electrons of energy E (GeV) the radiation pattern of figure 1a is thrown sharply forward in the direction of motion of the electron due to the relativistic Lorentz transformation from the rest frame of the electron to the laboratory frame. The resulting radiation pattern is shown in figure 3.

An observer in the laboratory looking along the tangent to the electron orbit would receive a pulse of radiation each time the electron passed by (akin to seeing periodically the headlights of a vehicle speeding around a circular race track). This pulse repeats at the orbital frequency of the electron. One might expect to observe the harmonics of this frequency, which is 1.76 MHz at the NSLS. However, due to the relativistic transformation the radiated power is shifted to very high frequencies in the x-ray region of the spectrum. In addition, the frequency distribution of the synchrotron radiation shows little trace of the orbital harmonic frequency. This is due to the fact that the radiating electrons differ slightly in velocity on account of betatron and synchrotron oscillations, thereby blurring the different frequencies into a continuum.

In order to estimate the highest frequency seen by the laboratory observer, we need to calculate the opening angle of the emitted cone of synchrotron radiation. Radiation emitted at an angle $\theta_c$ relative to the electron direction of motion in the rest frame of the electron is seen at a much smaller angle $\theta_L$ in the laboratory frame of reference. The transformation is given by:

$$\tan\theta_L = \frac{\sin\theta_c}{\gamma(\beta + \cos\theta_c)} \qquad (4)$$

where $\gamma = \frac{E}{mc^2}$. The largest half-opening angle of the cone as observed in the laboratory frame occurs for $\theta_c = 90°$, in which case:

$$\tan\theta_L = \frac{1}{\gamma\beta} \approx \frac{1}{\gamma} = \frac{mc^2}{E} \qquad (5)$$

At the NSLS, E = 2.5 GeV which gives a typical half-opening angle of the cone of only 0.2 mrad.[72]

As the electron travels along its circular arc, the narrow cone of synchrotron radiation produces a uniform time-averaged distribution of intensity in the orbital (horizontal) plane. Any unique angular distribution in this plane is lost and, instead, a fan of radiation several degrees wide is produced (from a single bending magnet of the accelerator). However, a strong angular dependence remains in the vertical direction. The vertical half-opening angle $\theta_v = \theta_L \approx \gamma^{-1}$ (eqn 5) gives the half-width of this angular distribution and applies to synchrotron radiation energies $E_x$ near the peak of the intensity versus energy curve. At lower energies off the peak, $\theta_v$ is greater than $\gamma^{-1}$. An approximate value is given by:

$$\theta_v(\text{mrad}) = \frac{0.51}{E}\left[\frac{E_c}{E_x}\right]^{0.38} \qquad (6)$$

where $E_c$ is the critical energy that characterizes the frequency distribution; half the total power is radiated above $E_c$ and half below. Lower values of $E_x$ correspond to larger opening angles.

Knowing $\theta_v \approx \gamma^{-1}$, we can calculate the short segment of the electron orbit from which the synchrotron radiation reaches the observer. Referring to figure 4 the duration $\Delta t$ of the pulse seen by the observer over this segment is:

$$\Delta t = \frac{s}{v} - \frac{d}{v} = \frac{2R}{c}[\theta_L - \sin\theta_L]$$
$$\approx \frac{2R}{c}\frac{\theta_L^3}{3!} = \frac{R}{c\gamma^3} \qquad (7)$$

A pulse of duration $\Delta t$ has frequency components up to:

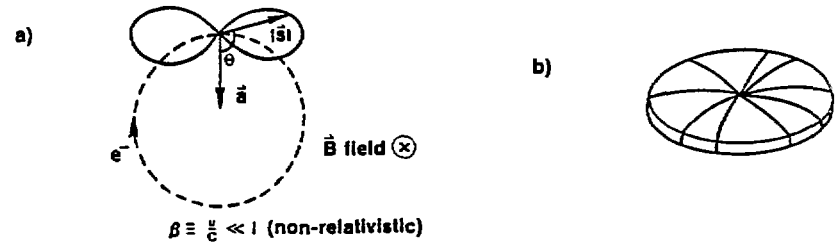


**Figure 1. Spatial distribution of the radiation pattern of non-relativistic electrons in circular motion.**
**a)2-dimensional, b)3-dimensional**

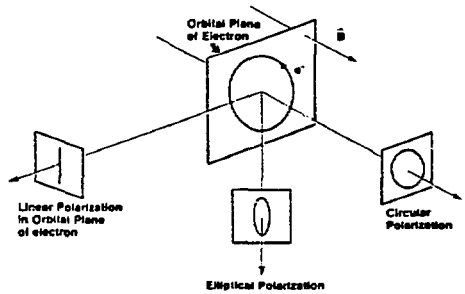


Figure 2. Polarization states of the radiation emitted by electrons in circular motion for different directions of observation.

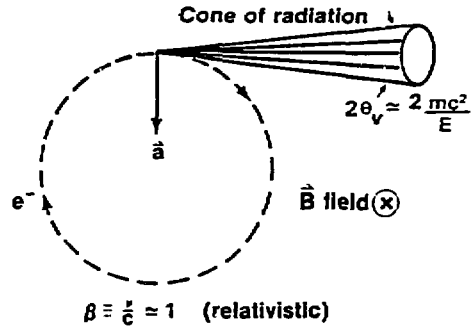


**Figure 3. Radiation pattern of relativistic electrons in circular motion.**

$$\omega_{max} = \frac{1}{\Delta t} = \frac{c\gamma^3}{R} \qquad (8)$$

with a corresponding energy of:

$$E_{max} = \hbar\omega_{max} = \frac{\hbar c\gamma^3}{R} . \qquad (9)$$

This qualitative analysis gives the $\gamma^3$ dependence of the maximum frequency and gives a photon energy which is close to the critical energy:

$$E_c(\text{keV}) = \frac{3}{2}\frac{\hbar c\gamma^3}{R} = 0.665\ BE^2 = 2.218\ \frac{E^3}{R} \qquad (10)$$

(See reference 73 page 15.)

For an electron of energy E = 2.5 GeV at the NSLS, we obtain $E_c$ = 5 keV for a B field of 1.22 T and 25 keV for a 6 T wiggler magnet. The latter energy corresponds to a harmonic which is $3 \times 10^{12}$ times the orbital frequency of the electrons in the accelerator ring. The relativistic relation for the radiated power is:

$$P = \frac{2}{3}\frac{e^2c}{R^2}\beta^4\left[\frac{E}{mc^2}\right]^4 \qquad (11)$$

Detailed calculations by Schwinger[63] show that the intensity of the synchrotron radiation rises with increasing photon energy $E_x$ until just below the critical energy. Figure 5 shows the photon intensity from the Stanford Positron Electron Asymmetric Ring (SPEAR), the Synchrotron Radiation Source (SRS), and the NSLS x-ray ring for a photon beam that includes the entire vertical opening angle and 1 mrad horizontal acceptance angle. The radiation extends over the infrared, visible, ultraviolet and x-ray regions of the spectrum.

Synchrotron radiation is in general elliptically polarized. However, as with cyclotron radiation, if the observer is located exactly in the plane of the electron orbit, the radiation is 100% linearly polarized with the electric vector in the instantaneous orbital plane.

Electron Storage Ring Accelerator

Table I lists the storage ring synchrotron radiation sources in operation or under construction as of late 1983.[2,71]

Figure 6 shows a view of a section of the 2.5 GeV storage ring at the NSLS showing bending and focussing magnets. Figure 7 is a schematic of a storage ring, where only the major components are shown. These include (a) an injector which allows electrons to enter the storage ring from a separate accelerator (not shown); (b) dipole bending magnets that constrain the electrons to the circular arcs from which the synchrotron radiation is emitted; (c) quadrupole magnets (one set shown) which focus the electron beam in the dipole bending magnets to a source size typically 0.3 mm high x 1.0 mm wide; (d) rf accelerating cavities (one shown) which replenishes the energy given up by the electron beam to synchrotron radiation; (e) optional insertion devices, such as a wiggler or undulator magnet for enhancing the synchrotron radiation intensity and energy. These devices are inserted in the straight sections between bending magnets and cause the electrons to curve back and forth and thus to radiate. By this process the energy spectrum of the emitted photons is shifted to higher energies. Figure 5 shows the increased photon intensities obtainable from a 6 pole, 6 T wiggler magnet at the NSLS. The wiggler spectrum represents the intensity per pole; with three electron oscillations the photon intensities are increased by about a factor of 5 over that shown in figure 5. The first wiggler went into regular use for experiments at the Stanford Synchrotron Radiation Laboratory (SSRL) in 1979; the first undulator in 1981; (f) oil-free vacuum pumps to evacuate the beam line to pressures of $10^{-9}$ torr or less. At these pressures hydrocarbon deposits on optical beam line

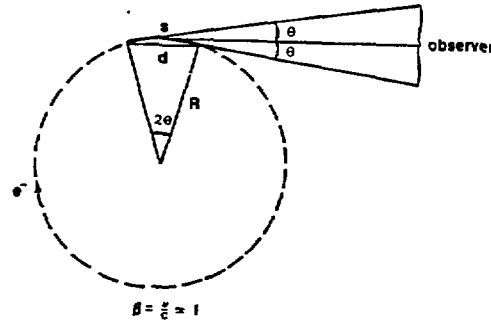


Figure 4. Segment of electron orbit from which synchrotron radiation reaches a laboratory observer (not to scale).

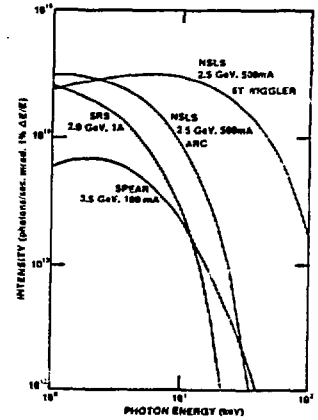


Figure 5. Photon intensities from SPEAR (Stanford), SRS (Daresbury), and NSLS X-Ray Ring (Brookhaven).

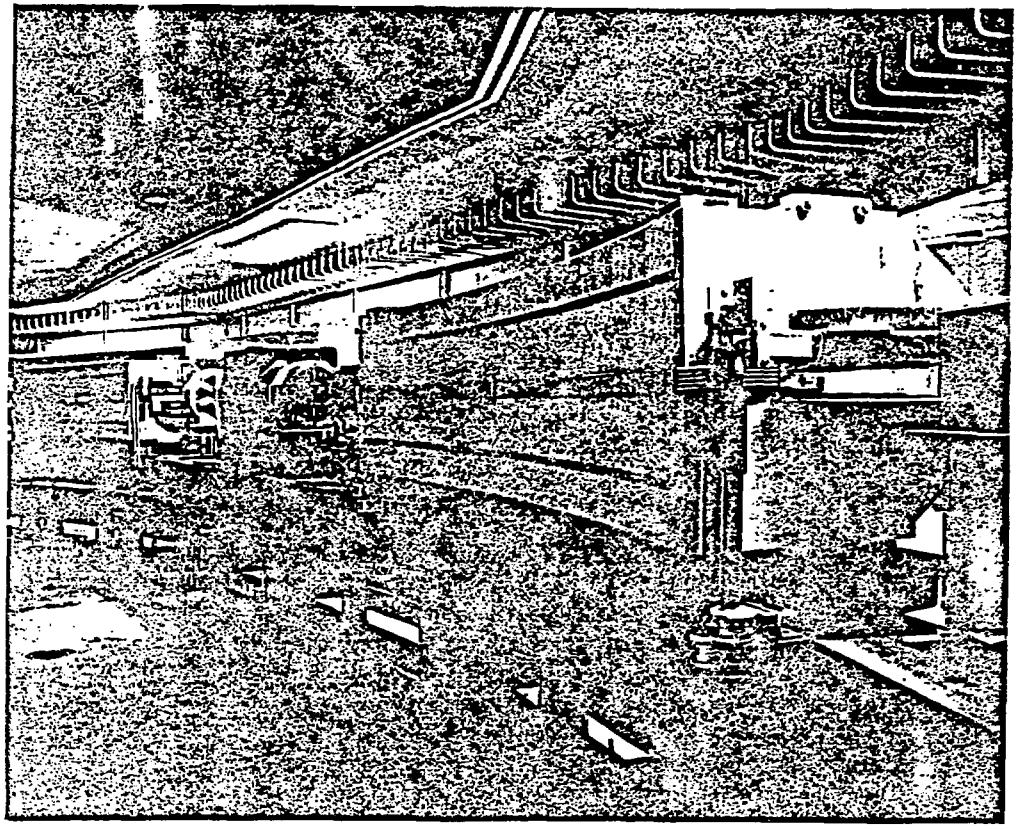

Figure 6. Photograph of a section of the x-ray ring at the NSLS showing dipole bending magnets (foreground and background) and quadrupole focussing magnets.

Table 1. Storage Ring Synchrotron Radiation Sources.

| Location | Ring (Lab) | Electron Energy (GeV) | Mode |
|---|---|---|---|
| China | | | |
| Beijing | BEPC (IHEP) | 2.2-2.8 | Parasitic+ |
| Hefei | HESYRL (USTC) | 0.8 | Dedicated+ |
| England | | | |
| Daresbury | SRS | 2.0 | Dedicated |
| France | | | |
| Orsay | ACO (LURE) | 0.54 | Dedicated |
| | DCI (LURE) | 1.8 | Partly dedicated |
| | Super ACO (LURE) | 0.8 | Dedicated+ |
| Germany | | | |
| Hamburg | DORIS (DESY) | 5.5 | Partly dedicated |
| West Berlin | BESSY | 0.8 | Dedicated |
| Italy | | | |
| Frascati | ADONE | 1.5 | Partly dedicated |
| Japan | | | |
| Tsukuba | Photon Factory (KEK) | 2.5 | Dedicated |
| | Accumulator (KEK) | 6-8 | Partly dedicated+ |
| | TRISTAN (KEK) | 30 | Parasitic+ |
| | TERAS (ETL) | 0.6 | Dedicated |
| Tokyo | SOR (ISSP) | 0.4 | Dedicated |
| Okasaki | UVSOR (IMS) | 0.6 | Dedicated+ |
| Sweden | | | |
| Lund | Max | 0.55 | Dedicated+ |
| United States | | | |
| Gaithersberg, MD | SURF (NBS) | 0.28 | Dedicated |
| Ithaca, NY | CESR (CHESS) | 5-5.5 | Parasitic |
| Stanford, CA | SPEAR (SSRL) | 3-3.5 | Partly dedicated |
| Stoughton, WI | Tantalus (SRC) | 0.25 | Dedicated |
| | Aladdin (SRC) | 1.0 | Dedicated |
| Upton, NY | NSLS I (BNL) | 0.75 | Dedicated |
| | NSLS II (BNL) | 2.5 | Dedicated |
| Funded | | | |
| Stanford, CA | Applied Physics Dept Stanford Univ. | 1.0 | Dedicated to FEL |
| Proposed | | | |
| Berkeley, CA | NCAM (LBL) | 1.3 | |
| Stanford, CA | PEP (SSRL) | 8-15 undulator | Parasitic |
| | (SSRL) | 2,6 | Dedicated |
| USSR | | | |
| Karkhov | N-100 (KPI) | 0.10 | Dedicated |
| Moscow | Kurchatov | 0.45 | Dedicated+ |
| Novosibirsk | VEPP-2M (INP) | 0.7 | Partly dedicated |
| | VEPP-3 (INP) | 2.2 | Partly dedicated |
| | VEPP-4 (INP) | 5-7 | Parasitic |

+In construction as of 1983.

elements, which reduce their efficiency and reflectivity, are minimized; (g) monochromator and beam line optical elements to select a specific energy from the broad spectrum of the synchrotron radiation. This is done by dispersing the "white" beam using crystals in the region above about 0.5-1.0 keV (and diffraction gratings at lower energies).

At the NSLS the design beam current of 500 mA at 2.5 GeV corresponds to $1.8 \times 10^{12}$ electrons (repetition rate 1.76 MHz). These electrons travel around the storage ring in a bunch. As many as 30 bunches can be accommodated at one time in the ring. One bunch gives a pulse of synchrotron radiation ≈0.7 ns long. For experiments dealing with fluorescence lifetime measurements and time-resolved spectroscopy, this time structure in the beam is highly useful.[54]

## Properties of Synchrotron Radiation Important for SXRF and EXAFS Analysis

### Intense, Monochromatic, Tunable

For the research to be described below, the most important property of synchrotron radiation is its continuous, high intensity spectrum. The intensity distribution shown in figure 5 ranges from the infrared to the hard x-ray region. As a rule the intensity is sufficient for most purposes up to energies five times $E_c$. This means that with the 1.22 T bending magnets at the NSLS the usable photon energies range through the K or L absorption edges of all elements in the periodic table. With the 6 T wiggler usable photon energies range through the K shell absorption edges of most elements and affords less ambiguous elemental identifications. Thus the fluorescence

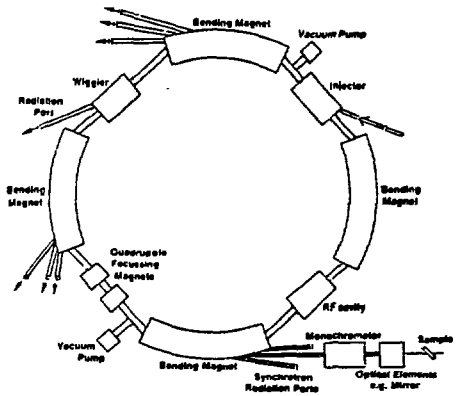


Figure 7. Schematic of an electron storage ring showing major components (see text).

from any given element can be selectively enhanced by tuning the monochromator to an energy just above the element's absorption edge. Beam energy resolutions of a few tenths of an eV are feasible.

The ability to tune the energy of the incident synchrotron beam allows the optimization of the detection limit for a given element, in particular for light elements such as Na, Mg, Al at the ppm level in a heavy matrix.

The high intensities of the synchrotron radiation are partly due to the fact that the source size in the bending magnet is small (for the NSLS the 4$\sigma$ size is 0.4 mm high x 1.3 mm wide) and that most of the radiation is emitted into a narrow cone of opening angle <1 mrad. The intensities of figure 5 are in marked contrast to that produced by an x-ray tube, which consists of a small number of discrete lines characteristic of the anode above a weak continuum. For experiments which call for a specific energy that is not any anode characteristic energy or for EXAFS experiments in which the energy dependence of the process is required, synchrotron radiation provides $10^2$ times the intensity at a characteristic x-ray line and $10^5$ times the intensity over the continuum when compared with a conventional x-ray tube.[21,8,56]

High Polarization

For SXRF and fluorescence EXAFS the high linear polarization of the synchrotron radiation in the electron orbital plane (horizontal) is of great use. This results from the fact that the main background to the fluorescence x-rays, which are emitted following the creation of inner-shell holes by the incident beam, arises from the Rayleigh and Compton scattering of the incident beam off the sample matrix. If the fluorescence x-ray detector is located in the plane of the electron orbit and at 90° to the incident synchrotron radiation beam, then a 100% linearly polarized incident beam would produce minimal Rayleigh or Compton background counts in the detector. This can be seen from the Rayleigh and Compton differential cross sections[36] for the scattering of photons off

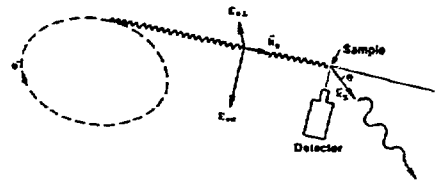


Figure 8. Schematic of photon scattering in the sample. $\vec{\epsilon}_{o\parallel}$ is the major polarization component of the incident radiation (of wave number $k_o$) in the orbital plane of the electron and $\vec{\epsilon}_{o\perp}$ is a small perpendicular component of polarization. The scattered photon has wave number $k_s$.

the electrons in the sample. (see figure 8):

$$\left(\frac{d\sigma}{d\Omega}\right)_{\text{Rayleigh}} = \begin{cases} r_s^2 \,|\vec{\epsilon}_s^{\,*} \cdot \vec{\epsilon}_o|^2 \,|\, F(\vec{q},Z)|^2 \\ r_s^2\,(\cos^2\theta\cos^2\phi + \sin^2\phi)\,|\,F(\vec{q},Z)\,|^2 \end{cases} \quad \begin{matrix} \\ \text{for linearly polarized photons} \end{matrix} \tag{12}$$

$$\left(\frac{d\sigma}{d\Omega}\right)_{\text{Compton}} = \begin{cases} r_s^2\left(\frac{k_s}{k_o}\right)^2 \left[|\vec{\epsilon}_s^{\,*} \cdot \vec{\epsilon}_o|^2 + \frac{(k_o - k_s)^2}{4k_o k_s}\right] S(\vec{q},Z) \\ \tfrac{1}{4} r_s^2\left(\frac{k_s}{k_o}\right)^2 \left[\frac{k_o}{k_s} + \frac{k_s}{k_o} - 2 + 4\cos^2\eta\right] S(\vec{q},Z) \end{cases} \quad \begin{matrix} \\ \text{for linearly polarized photons} \end{matrix} \tag{13}$$

where $r_o$ is the classical electron radius, $\vec{\epsilon}_o$ is the polarization of the incident photon of wave number $k_o$, $\vec{\epsilon}_s$ is the polarization of the scattered photon of wave number $k_s$, $F(\vec{q},Z)$ is a form factor which represents the probability that a momentum $\vec{q}$ is transferred to the Z electrons of the atom without any energy absorption,

$$\frac{k_s}{k_o} = \frac{1}{1 + \frac{E_x}{mc^2}(1 - \cos\theta)} \quad \text{(Compton formula)},$$

$S(\vec{q},Z)$ is the probability that an atom will be raised to an excited or ionized state, $\phi$ is the angle between the direction of polarization of the incident photon and the direction of observation, $\eta$ is the angle between the polarization directions of the incident and scattered photons, $\theta$ is the scattering angle i.e., the angle between the incident photon direction and the direction of observation. From equations (12) and (13) for linearly polarized incident photons ($\epsilon_{o\parallel} \neq 0$, $\epsilon_{o\perp} = 0$) both the Rayleigh and Compton scattering cross sections are minimized by placing the detector at $\theta = 90°$ and in the ($\epsilon_{o\parallel}$, $k_o$) plane. In practice a solid state x-ray detector subtends a finite solid angle and the incident synchrotron radiation beam is not 100% linearly polarized, which nevertheless makes for a ten-fold increase in the signal to background ratio in comparison to conventional tube excited XRF.[6,66] Figure 9 adopted from Jones et al[40] shows the rapid increase in the

Rayleigh and Compton background events as a function of distance from the orbital electron plane. It indicates the importance of positioning the x-ray detector carefully to take maximum advantage of the synchrotron radiation polarization.

The Rayleigh and Compton scattered radiation reaching the solid state detector is degraded in the diode by insufficient charge collection[25] to become the major component of the background underneath the fluorescence x-ray signal. The background is largest for samples with low Z matrices. Sparks[66] reported that for samples with $Z \leq 8$ the solid state detector's contribution to the background was ≈ 90% of the total background. This percentage dropped to 30% for Z = 14 (Si) and 5% for Z = 82 (Pb).

In principle, a greater than 10-fold increase in the signal to background ratio mentioned above could be achieved with narrow strip solid state detectors, which lie essentially only in the electron orbital plane, or with a wavelength dispersive detector. Stern and Heald[69] have suggested a novel scheme of filters and Soller-type slits which substantially reduces the background counts and is simpler than inserting a wavelength dispersive spectrometer.

The option of eliminating the background in SXRF is in contrast to analyses using electron and proton excitation. In charged particle excitation, the background is due mainly to secondary electron bremsstrahlung in the sample, which is difficult to separate from the fluorescence signal.

Natural Collimation

For many purposes a small beam spot on target is of value. Since most of the synchrotron radiation is emitted in an extremely narrow cone, very high intensities are possible at large distances (≈ 25 m) from the storage ring on targets as small as 1 mm in height.

High Vacuum Environment and Stability

For most surface EXAFS experiments aimed at studying corrosion, segregation of elements near a surface, etc., the ultrahigh vacuum environment of the storage ring is important to ensuring contamination-free surfaces.[3] At $10^{-9}$ torr or less elements such as oxygen and carbon can be studied. In addition, since the lifetime of the stored electron beam varies inversely as the average pressure, the ultrahigh vacuum ensures stability of the intensity and energy of the synchrotron radiation over periods of several hours.

Problem Areas: Alignment and Higher Order Radiation

The use of synchrotron radiation is not without its practical problems. The first difficulty that the user-experimenter must face is the alignment of the beam line components i.e., monochromators, mirrors, etc., and the target chamber. In most cases, ready access to the beam line components is not possible due to the harmful x-rays present. It is common practice to use a laser for initial alignment of the components and fluorescent zinc sulfide screens for the final adjustments. During operation of the storage ring, small vertical angular deviations of the electron beam can result in deviations of a millimeter or more at the target. Therefore, position monitors with feedback signals are used to "lock" the synchrotron radiation onto the target. Misalignment can cause a) higher background and b) "contamination" of the characteristic peaks in the x-ray spectrum; these considerations are important particularly at the ppm and ppb levels of analysis.

One of the most serious problems for many experiments is that of removing higher order radiation from the monochromatized beam. For uv and soft x-rays, selective reflections and filters have been used.[12] For x-rays Bonse et al[5] have suggested ways of eliminating higher order harmonics by making a double crystal monochromator system "slightly dispersive." In the last five years major improvements in the construction of two crystal monochromators have taken place.[32,47,9,48,51,4,26] Sayers et al[61] have designed a unique 4-crystal monochromator for x-ray absorption studies at the NSLS. In a recent experiment at CHESS[11,30] a single crystal monochromator was detuned to decrease the intensity of the higher order radiation; however, there was a loss in intensity at the primary energy. Finally, the problem can also be handled by using a wiggler or undulator magnet.[43]

## Selected Applications of Synchrotron Radiation

### Synchrotron X-Ray Fluorescence (SXRF)

With the continued advance of experimental techniques it is now possible to analyze the elemental composition of a material using electrons, protons, heavy ions and photons (x-rays). X-rays are unique among this group in that their interactions with atoms exhibit sharp peaks. Figure 10 shows the photoelectric cross sections for $Ca^{20}$ and $Pb^{82}$ as a function of photon energy. The peaks occur in the energy region where the photoelectric cross section for the creation of an inner-shell vacancy goes from zero to its maximum value as the incident photon energy is increased above a threshold value necessary to eject the bound electron. Thus a unique resonance exists with each electron energy level that is not available with the other particles. The sharp resonances account for the attractiveness of the x-ray fluorescence technique for elemental analysis.

One can make use of the fact that, after the creation of an inner-shell hole, the corresponding yield of fluorescence x-rays will increase significantly for a small change in the incident x-ray energy near the absorption edge of the inner shell. By correlating the sharp rise in fluorescence with the incident x-ray energy near the absorption edge, the element can be identified in an unequivocal way.

Synchrotron radiation offers a broad continuous spectrum of x-rays from which any excitation energy can be selected with a monochromator. In addition, x-rays have fluorescence cross sections $10\text{-}10^3$ times higher and fluorescence signal to background ratios $10\text{-}10^3$ times larger than electrons or protons. X-rays also deposit $10^{-3}$ - $10^{-5}$ as much energy in the sample for the same minimum detectable limit (MDL). These estimates imply in general lower MDL's and reduced heat and

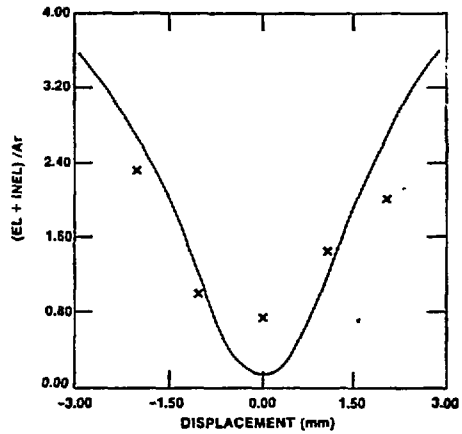


Figure 9. Intensity distribution of Rayleigh and Compton scattering as a function of distance from the electron orbital plane. The solid curve is the calculated polarization assuming an electron beam of negligible height. The crosses are experimental data values. Adapted from Jones et al. (Ref. 40)

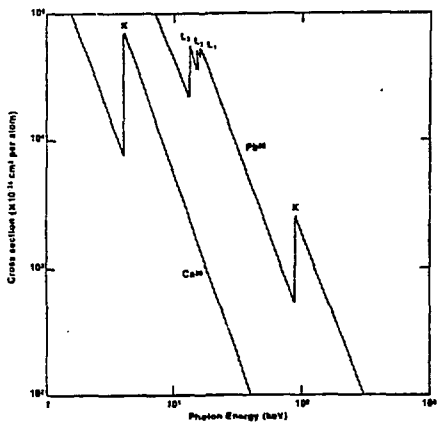


Figure 10. Photoelectric cross sections for $Ca^{K}$ and $Pb^{M}$ versus photon energy.

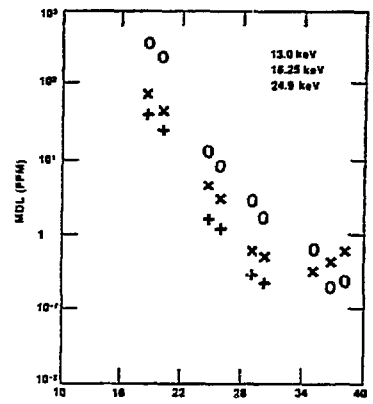


Figure 11. Minimum detectable limits of several elements in NBS Orchard Leaves when fluoresced with 13.0, 16.25 and 24.9 keV x-rays. Adapted from Hansen et al. (Ref. 30)

radiation damage to the material under study depending upon the experimental conditions.

One of the noteworthy applications of SXRF was reported in 1977 and 1978 by Sparks et al[68,67] in a search for primordial superheavy elements in giant-halo monazite inclusions in biotite mica. Earlier Gentry et al[20] had interpreted the proton induced x-ray emission (PIXE) spectra of the same and other inclusions as possibly containing the characteristic $L\alpha_1$ line of the Z = 126 superheavy element. Other superheavy elements could be associated with weaker lines, although only one spectral line was observed for each reported element. Because of fifth-period K lines and proton induced nuclear reactions,[19,18] a unique interpretation of the PIXE spectra was not possible.

The SXRF experiment of Sparks et al used a curved graphite monochromator which could be tuned to an energy near the 36 keV $L_3$ absorption edge predicted for the Z = 126 superheavy element. The fluorescence x-rays were detected by a Si(Li) detector located in the plane of the electron orbit and at 90° to the incident synchrotron radiation beam. An MDL of $5 \times 10^8$ atoms of element Z = 126 could have been detected during an 8 h run. This was 55 ± 10 times fewer atoms than could have been detected in the PIXE experiment. The SXRF experiment showed conclusively that superheavy elements were not present in any of the inclusions at the above MDL.

Minimum Detectable Limit. A number of measurements of the MDL's feasible with the SXRF technique have appeared in the literature. Il'in et al[35] reported MDL's of 16 ppb for Zn and 72 ppb for Au in aqueous solutions in 1000 s runs. Sparks[66] measured MDL's in 100 s using National Bureau of Standards (NBS) reference materials for 37 keV synchrotron radiation. The results were, for example, $10^{-11}$ g for V (Z = 23) and $3 \times 10^{-13}$ g for Cd (Z = 48), which compares favorably with PIXE MDL's of $4 \times 10^{-12}$ g for V and $1 \times 10^{-11}$ g for Cd.[39] More recently, detailed studies of the MDL's were reported by Hanson et al[30] for three incident energies ($E_x$ = 13.0, 16.25, and 24.9 keV) at the Cornell High Energy Synchrotron Source (CHESS). The results for several elements in 1 mm thick samples of pressed NBS orchard leaves obtained in 300 s are shown in figure 11. Figure 12 shows results of Bos et al[6] including a comparison with tube excited XRF and PIXE MDL's. Thin targets (≈ 5 mg/cm$^2$) of NBS orchard leaves were irradiated for 1000 s using 9.1 and 16.5 keV synchrotron x-ray energies at SRS (Daresbury).

Gilfrich et al[21] have made a systematic study of the MDL's for 10 elements using a continuum synchrotron beam of energy 2-60 keV. Both energy dispersive and wavelength dispersive measurements were made. The results range from $10^{-3}$ to $10^{-1}$ μg/cm$^2$. When the beam size is taken into account, absolute MDL's of $10^{-12}$ to $10^{-11}$ were obtained. Similar values for the absolute MDL's have also been reported by Knöchel et al,[42] who optimized the MDL for a given element by using different absorbers in the primary beam.

A number of experimental programs are currently underway to make use of SXRF for various elemental analyses. Chen et al[11] are studying coal and other geological materials. The first experiment examined the variations with depth of the elemental concentrations in coal vitrinites at CHESS. Figure 13 shows a schematic of the crystal cave housing the monochromator and the A2 experimental hutch containing the target detector assembly. The Si(Li) detector (not shown) was placed in the electron orbital plane and at 90° to the beam. Figure 14 shows the SXRF spectrum from coal vitrinite no. 43.52 m. The experimental results confirmed the trend of increasing Fe concentrations with depth into the coal bed that was established by Minkin et al[52] using PIXE techniques. In addition, the S concentrations were found to decrease from top to bottom of the bed in contrast to the Fe concentrations.

Davies et al[15] have studied the quantification of implanted species in semiconductor substrates and the trace element content of high-purity galium and arsenic. Arsenic implanted silicon and copper implanted cadmium telluride specimens were analyzed by a synchrotron radiation beam with a 1 mm$^2$ cross sectional area. In 100s $6 \times 10^{13}$ As ions cm$^{-2}$ and $2 \times 10^{14}$ Cu ions cm$^{-2}$ were detectable. Figure 15 shows the cadmium telluride spectrum for an incident synchrotron radiation energy near 19 keV. The cadmium Kα line at 23.11 keV was excited by the second harmonic of the incident beam.

Several biological studies have been made using SXRF techniques. Jones et al[40] examined the radiation damage effects of white radiation on the morphology of human blood cells and other types of tissues. Hanson et al[29] have investigated chromium and nickel trace concentrations in yeast. Prins et al[59] have studied human hair using both white radiation and monochromatized beams.

Extended X-Ray Absorption Fine Structure (EXAFS): Conventional Detection

One of the most exciting results of the availability of x-ray synchrotron radiation is the development of the EXAFS technique by which the coordination of an individual element in a complex material can be determined. By coordination is meant the type and geometric arrangement of the atoms surrounding the element being detected. Such information is useful in characterizing the chemical state of the element and is usually obtainable only with other less sensitive techniques which are also destructive.

EXAFS refers to the small variations or fine structure in the x-ray absorption coefficient μ of a polyatomic material as the energy of the incident x-ray is varied from just below to approximately 1000 eV above the K or L absorption edges of a specific element in the material. Figure 16 shows a schematic of the x-ray absorption spectrum near a K shell absorption edge. Below the K shell binding energy the 1S electron is excited to unoccupied higher energy levels. These transitions produce a series of discrete but very closely spaced lines in the photoelectric absorption spectrum. When $E_x$ is equal to the K shell absorption energy, the 1S electron

can be excited to the continuum and a sharp increase in the cross section is observed. As $E_x$ is increased further, damped oscillations in the cross section occurs. These oscillations or fine structure extend to ≈1000 eV above the K shell binding energy.

The absorption coefficient $\mu$ of a compound material of mass density $\rho$ contains contributions from the constituent elements, i.e.,

$$\frac{\mu}{\rho} = c_1(\frac{\mu}{\rho})_1 + c_2(\frac{\mu}{\rho})_2 + \ldots c_\ell(\frac{\mu}{\rho})_\ell + \ldots \quad (14)$$

where $c_\ell$ is the concentration of element $\ell$. When an x-ray of energy $E_x$ is absorbed by a K shell electron of element $\ell$, the momentum p of the resulting photoelectron is given by:

$$\frac{p^2}{2m} = E_x - E_K \quad (15)$$

where $E_K$ is the K shell absorption edge. The photoelectron wave vector k is obtained from the deBroglie relation:

$$p = \frac{h}{\lambda} = \hbar k \quad (16)$$

Each mass absorption coefficient $(\frac{\mu}{\rho})_\ell$ is proportional to the square of the probability amplitude that describes the transition from the initial state $\Psi_i$ (consisting of a synchrotron photon and a K shell electron) to the final state $\Psi_f$ via the photon-electron interaction $H_{int}$,

$$(\frac{\mu}{\rho})_\ell \propto |\langle\Psi_f|H_{int}|\Psi_i\rangle|^2 \quad (17)$$

The final state is that of the ejected photoelectron with wave vector k, which is represented by a spherical wave $e^{ikr}$ expanding in the lattice and a backscattered wave $\Psi_s$ representing the backscattering of the photoelectron by neighboring atoms surrounding element $\ell$,

$$\Psi_f = e^{ikr} + \Psi_s \quad (18)$$

There is constructive or destructive interference of the outgoing and backscattered waves at the site of the ionized atom depending on the value of k. When $E_x$ is varied, k changes. This results in alternations of the constructive and destructive interference pattern, which gives rise to the modulation or fine structure in $(\frac{\mu}{\rho})_\ell$ and hence in $\mu$ of the material. Because $\Psi_s$ depends on the coordination (number, type, distance) of nearby atoms surrounding element $\ell$, measurement of the fine structure yields information on the chemical form of the element.

EXAFS has been recognized for some fifty years, but it was not until the pioneering work of Sayers et al[62] and the advent of synchrotron radiation sources that its use became widespread. The expression for the modulation of the absorption coefficient is given by[1,46]

$$\frac{\mu - \mu_o}{\mu_o} = \chi(k) = \sum_j \frac{N_j}{kR_j^2} |f_j(k)| e^{-2\sigma_j^2 k^2} e^{-R_j/\lambda(k)} \sin[2kR_j + \phi_j(k)] \quad (19)$$

where $f(k)$ is the amplitude of the backscattered wave and $\phi(k)$ the phase shift. $N_j$ is the number of atoms in a coordination shell at average distance $R_j$, and $\sigma_j$ is the mean square deviation of $R_j$. The term $e^{-2\sigma_j^2 k^2}$ leads to the damping of the oscillation, and the term $e^{-R_j/\lambda(k)}$ gives the EXAFS technique its local characteristics due to the short (few Å) mean free path $\lambda(k)$ of the photoelectron.

In its simplest form the EXAFS process is put to use by first determining the line shape and the position of the absorption edge of a particular element. This is done by monitoring the ratio of transmitted to incident beam $[\frac{I}{I_o} = e^{-\mu(k)x}]$ as the incident photon energy $E_x$ is varied. The results are then compared with those of model compounds covering the range of chemical states of the element in question.

Figure 17 shows a schematic of the apparatus used for studying EXAFS. A high resolution monochromator is used to select $E_x$ and ionization chambers are placed appropriately to measure $I_o$ and I. The x-ray fluorescence detector is used in the fluorescence EXAFS mode (see below).

Cramer et al[14,13] have applied the above technique to determine the chemical state of molybdenum in nitrogenase. A linear correlation was established between the "chemical shift" of the Mo K edge and the calculated coordination charge for a wide range of Mo compounds. Mo in resting nitrogenase and Mo in oxo-bridged Mo(V) cysteine complex were found to have the same chemical shift. This result suggested that the oxidation state for Mo in the enzyme is Mo(V). Recently Wong[74] and Greaves et al[27] have reported EXAFS studies on metallic glasses.

Extended X-Ray Absorption Fine Structure (EXAFS): Fluorescence Detection

If the concentration $c_\ell$ in equation (14) is small, then changes in $(\frac{\mu}{\rho})_\ell$ become difficult to detect by a measurement of $\mu$ for the entire material as is done in a transmitted beam experiment. However it was soon realized that any process whose probability amplitude depends on the same transition $\langle\Psi_f|H_{int}|\Psi_i\rangle$ will also exhibit EXAFS. For example EXAFS-type oscillations have been found in x-ray fluorescence, Auger, photo- and secondary electron emission, secondary ion emission, photon stimulated desorption, Mossbauer spectroscopy and possibly other phenomena.

For x-ray fluorescence EXAFS the fine structure in the spectrum of element $\ell$ as a function of incident energy $E_x$ is especially pronounced because the contributions of other elements to the fluorescence spectrum is negligible, when $E_x$ is near the K or L absorption edges of element $\ell$. Thus fluorescence detection is $\approx 10^3$ times more sensitive for following EXAFS oscillations than measuring the ratio $I/I_o$. At present chemical speciation experiments using fluorescence EXAFS

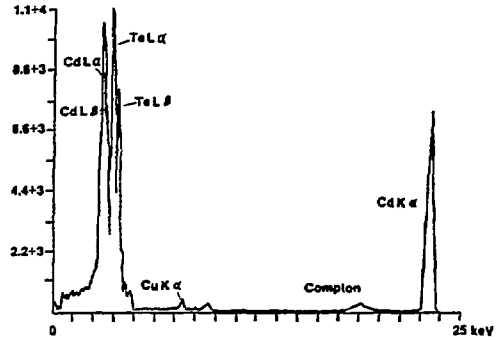


*Figure 15. SXRF spectrum of Cu-implanted cadmium telluride. Adapted from Davies et al.* (Ref. 15)

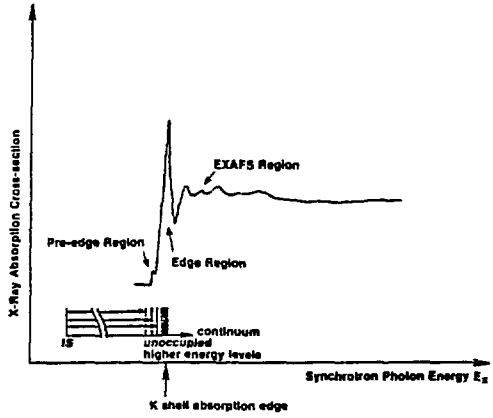


Figure 16. Schematic of the x-ray absorption spectrum showing the pre-edge, edge and EXAFS regions.

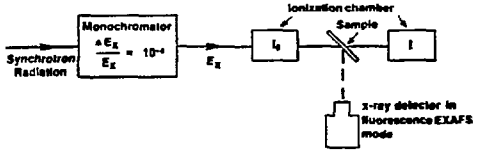


*Figure 17. Schematic of EXAFS apparatus.*

are being performed for elements at the 10 ppm concentration level.

In 1977 Jaklevic et al[37] was the first to report a quantitative comparison between fluorescence EXAFS and direct absorption techniques. They showed that the two methods yielded essentially the same information as shown by the almost identical spectra in figure 18. However the sensitivity of the SXRF technique was found to be $>10^2$ times more sensitive. This allowed the study of more dilute systems and thinner films than were possible with the direct absorption technique. For example, figure 19 shows the fluorescence abosrption spectrum of Mn at 10-50 ppm in a leaf. The transmitted beam technique gave negative results. In a later study Jaklevic et al[38] have extended the above measurements to the chemical characterization of air environmental samples.

An important application of the fluorescence EXAFS technique was reported recently by Maylotte et al,[49] who showed that the trace vanadium in coal (Kentucky no. 9 seam) exists in at least two environments, in both of which it is coordinated to oxygen. Figure 20 shows the fluorescence EXAFS spectra of a series of vanadium model compounds. Figure 21 shows the spectra of vanadium in coal, its sink and float fractions, and its liquefaction residue. Relative to raw coal, the float and sink fractions have different peak heights, which indicates the presence of more than one environment for vanadium in this coal. The heavy fraction spectrum appears similar to roscoelite or $V_2O_3$, that is $V^{3+}$ in octahedral oxygen coordination. Vanadium in the light fraction was found to be in agreement with a $V^{4+}$ assignment. In addition, the spectrum of the liquefaction residue is different from that of the raw coal and indicates that the vanadium environment was reduced to a trivalent state like that in $V_2O_3$ or roscoelite.

A detailed deconvolution of the fine structure oscillations in the coal spectra was also carried out to determine the type and geometric arrangements of the atoms nearest to the vanadium. After Fourier transforming the oscillations in the spectrum and fitting various coordination configurations, it was established that vanadium is coordinated to oxygen and not to sulfur or nitrogen. These results have important implications for coal cleaning and conversion processes through their effects on corrosion, catalyst poisoning and environmental emissions.

Similar analyses have also been carried out for biological and chemical materials including rubredoxin by Shulman et al,[64] and several other metalloenzymes and metalloproteins.[16]

In summary, fluorescence EXAFS yields valuable information on the chemical state of an element in a complex polyatomic dilute material. Absorption edges corresponding to several elements can be measured in the same material. In addition the method is a non-destructive one that does not require a vacuum nor any sample preparation which might disturb the elemental environment in the material.

## Future Applications

This section deals with new developments in SXRF and fluorescence EXAFS, which indicate some of the applications which are currently being formulated. In particular we shall describe the capabilities of the new x-ray fluorescence microprobes for elemental analysis.

### New Trends in Fluorescence EXAFS

As described above, information from an EXAFS experiment can be obtained by simply comparing the absorption edge position and the magnitude of the fluorescence signal with those of model compounds. Additional information can be obtained by analyzing the Fourier transform of the fine structure oscillations. In recent years more accurate calculations of the amplitude and phase of the backscattered wave,[45] combined with attempts to describe the scattering in terms of curved waves[55] instead of the plane wave approximation, have spearheaded attempts to describe complex materials without resorting to model compounds. Phenomenological prescriptions which have been arrived at from measurements of model compounds are now being replaced by more fundamental descriptions of the electron-photon and electron-atom interactions. Many of the new theoretical calculations are being tested using x-ray absorption near edge spectroscopy (XANES),[41] which gives information on the symmetry of the coordination environment of a given element.

### X-Ray Fluorescence Microprobe

Knowledge of the elemental concentrations in micrometer-size samples is of interest in many scientific applications. In addition, a map of the distribution of the elements over a sample, which can be obtained by scanning the sample across the microprobe, provides useful information. An example of this occurs in the study of coal, where an overall chart of the elemental concentrations in specific macerals and fine-grained minerals is needed to advance the theory of the paleo-geochemical history of the coal.[76,31,53]

X-ray fluorescence microprobes currently under construction at various synchrotron radiation laboratories possess many advantages over the electron and proton microprobes used for elemental analysis. These advantages have been well documented by Gordon,[23,24] Grodzins,[28] and Sparks.[66] Briefly, they include: (i) higher signal to background ratio. The fluorescence S/B ratio from x-ray excitation is $10^2$-$10^3$ times greater than that from electron excitation and 10 times greater than that from proton excitation; (ii) lower energy deposition. X-rays deposit $10^{-3}$-$10^{-5}$ times as much energy in the sample for the same elemental detectability compared with electrons and protons. Thus the likelihood of breaking chemical bonds, redistributing and/or volatilizing susceptible elements e.g., Br, As, etc., is less with x-ray excitation; (iii) favorable operating conditions. Analysis of samples with x-rays can be carried out in a non-vacuum environment e.g., in air, helium, aqueous surroundings, etc.; (iv) lower minimum detectable limits. Under optimum conditions MDL's as low as 10 ppm can be achieved with electron microprobes,[50] however in routine analysis for most

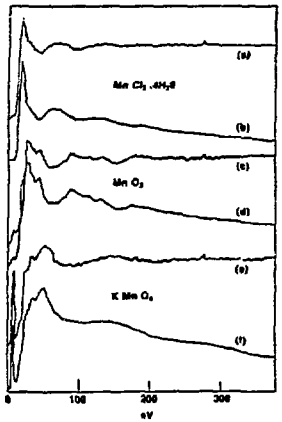


Figure 18. Comparison of fluorescence detection (a,c,e) with normal transmission studies (b,d,f) of the EXAFS structure of concentrated Mn in three different systems. Adapted from Jaklevic et al. (Ref. 37)

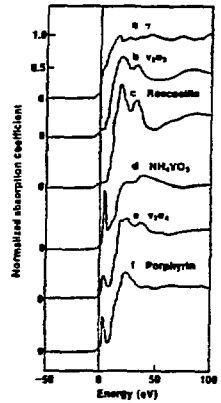


Figure 20. Vanadium K-edge absorption spectra for (a) metal, (b and c) octahedral coordination, (d) tetrahedral coordination, and (e and f) square pyramid coordination. Roscoelite is a vanadium mineral with the formula $KAl_2V_3Si_3O_{10}(OH)_2$. Adapted from Maylotte et al. (Ref. 49)

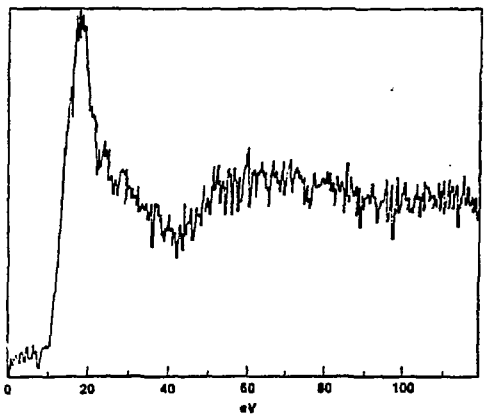


Figure 19. The absorption spectrum of Mn in a leaf taken by fluorescence detection. Adapted from *Jaklevic et al.* (Ref. 37)

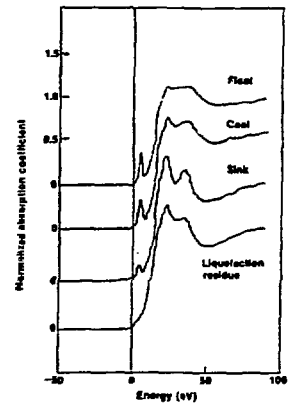


Figure 21. Vanadium K-edge absorption spectra in coal, its sink and float fractions, and its liquefaction residue. Adapted from Maylotte et al. (Ref. 49)

elements the practical lower limit of detection is about 100 ppm.[60] With a proton microprobe detection limits of about 1-10 ppm have been reported;[10] lower limits are expected when all experimental parameters are optimized. The first synchrotron x-ray fluorescence microprobe was constructed in 1972 by Horowitz and Howell[33] at the now defunct Cambridge Electron Accelerator. A condensing mirror intercepted the synchrotron radiation and focussed it down to a spot ≈1 x 2 mm$^2$. No attempt was made to form a focussed x-ray image. Instead a microbeam was obtained by using a pinhole collimator in a thin gold substrate. A 2 μm resolution was achieved. Gas filled proportional counters surrounding the sample detected the fluorescence x-rays. Calculations indicated that $10^{-6}$ - $10^{-9}$ g/cm$^2$ of an element was detectable at that resolution.

The x-ray beam constructed by Sparks et al[67] used a pyrolytic curved graphite monochromator to produce 37 keV x-rays into a spot ≈0.8 mm wide x 0.45 mm high at the sample. This arrangement achieved a minimum detectable limit of 10 ppb in a 0.5 mm$^2$ area.

More recent designs of x-ray fluorescence microprobes for elemental analysis employ focussing elements to form an image of the x-ray source. Figure 22 is a schematic of the experimental set-up under construction at the SRS (Daresbury).[58] Synchrotron radiation is emitted from the electron source of size 0.4 x 1.3 mm$^2$ and intercepted by a diaphragm before being brought to a focus at the sample by an ellipsoidally bent Si crystal. Calculations indicate that a 50 x 50 μm$^2$ beam size will contain a photon flux of 4.1 x $10^6$ photons/s/μm$^2$, which is sufficient to obtain an MDL of 1 ppm in a 5 s per pixel measuring time.

Figure 23 shows a schematic of the microprobe beam line designed by Howells and Hastings[34] and now under construction at the NSLS. A multilayer two crystal monochromator is followed by an ellipsoidal or toroidal mirror to produce the focussed spot. It will be possible to interchange the multilayers with perfect crystals for high energy resolution fluorescence EXAFS work. During the initial phase-in operation of the x-ray storage ring, 10 mA electron currents at 2.5 GeV is expected. A spot size of 30 μm diameter with 4 x $10^{10}$ photons/s is planned during initial tune-up. This intensity should be increased by a factor of 50 when the storage ring is operational at its design current of 500 mA. In addition, beam spots of 1-10 μm with sufficient intensity to reach the 1-10 ppb level are then feasible. Assuming a standard arc source (bending magnet), the x-ray energy range covers $E_X$ = 2-16 keV, $\Delta E_X/E_X$ = 1-2%, which encompasses the K or L absorption edges for elements up to Pb. At a later stage when a wiggler magnet is inserted, resolutions <1 μm for energies >100 keV become feasible.

Grodzins[28] has calculated the minimum detectable limit for Zn in a 1 mg/cm$^2$ carbon matrix for a similar microbeam containing 5 x $10^9$ photons/μm$^2$ in a 1% bandwith. Using a wavelength dispersive detector with a 50 eV resolution, he estimated that for 100 s irradiation the MDL's are 70 ppb, 3 ppb and 0.5 ppb for beam spot diameters of 1 μm, 5 μm and 30 μm, respectively; (v) a disadvantage of x-ray fluorescence microprobes, compared to electron and proton microprobes, is the much higher penetrating depth of x-rays. In carbon a 15 keV electron has a range of 2.5 μm; a 3 MeV proton has a range of 73 μm; whereas a 20 keV x-ray has a mean free path of about 1 cm. The consequent lower depth resolution for x-ray microprobes can be compensated by using thin targets and a higher incident x-ray flux. Under such experimental conditions, the advantages described in (ii) and (iv) above would be reduced.

Energy-Dispersive EXAFS and Scanning X-Ray Fluorescence Microprobe

An experimental technique, which is being considered for elemental and chemical analyses, uses a curved crystal to focus a parallel white beam of synchrotron radiation onto the sample (figure 24). Since each part of the crystal reflects only one energy corresponding to the correct Bragg angle, energy dispersion of the beam is produced. After passing through the sample, the energy dispersed x-rays diverge and are detected by a position sensitive detector or x-ray film, with position corresponding to x-ray energy. An absorption spectrum can be obtained in a relatively short time. Time-dependent structural and chemical changes in a material can be studied.[57] Plans for such a scanning x-ray microprobe have been considered at SRS Daresbury. However further progress must await the availability of a wiggler beamline since very high incident beam intensities are required.[7]

## Conclusions

The fields of SXRF and fluorescence EXAFS are undergoing rapid development with the advent of new dedicated synchrotron radiation sources; several noteworthy experiments have been performed using these techniques. Future applications promise relatively complete chemical characterization of complex polyatomic materials by a combination of SXRF, which gives the elemental concentrations, and fluorescence EXAFS, which gives the chemical form of the elements. X-ray fluorescence microprobes under construction hold out the promise of 1 μm spatial resolution at minimum detectable limits of a few ppb - a new level of analyzing capability.

## Acknowledgements

This work was supported in part by the Geneseo Foundation, State University of New York, and the Processes and Techniques Branch, Division of Chemical Sciences, Office of Basic Energy Sciences, US Department of Energy, Contract No. DE-AC02-76CH00016.

## References

1. Ashley CA, Doniach S. (1975). Theory of extended x-ray absorption edge fine structure (EXAFS) in crystalline solids. Phys. Rev. B11, 1279-1288.

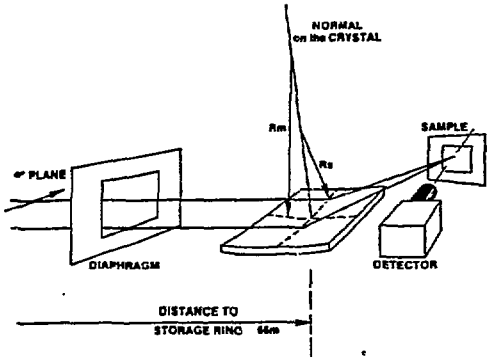


Figure 22. The simplified experimental set-up for trace element analysis with a focussed synchrotron radiation beam. The focussing crystal is situated in the plane of the storage ring and the detector perpendicular with the diffraction plane. Adapted from Price et al. (Ref. 58)

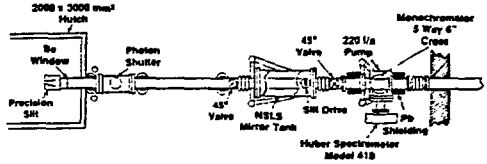


Figure 23. NSLS X-Ray Microprobe Beam Line.

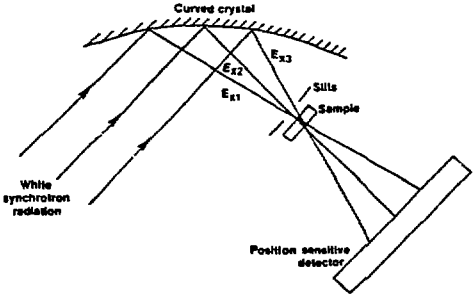


Figure 24. Schematic of scanning x-ray microprobe

2. Bienenstock A, Winick H. (1983). Synchrotron Radiation Research. Physics Today, June 1983, 48-58.

3. Boller K, Haelbich R, Hogrefe H, Jark W, Kunz C. (1982). Investigation of Carbon Contamination of Mirror Surfaces Exposed to Synchrotron Radiation. DESY SR-82-18, October 1982, 1-33. Available from: Deutsches Elektronen Synchrotron, Bibliothek, Notkestrasse 85, 2 Hamburg 52, West Germany.

4. Bonse U, Fisher K. (1981). The New Multi-Purpose Two-Axis Diffractometer for Synchrotron X-Rays at DORIS. Deutsches Elektronen-Synchrotron, DESY SR-81/12, October 1981, 1-38. Available from: Deutsches Elektronen Synchrotron, Bibliothek, Notkestrasse 85, 2 Hamburg 52, West Germany.

5. Bonse U, Materlik G, Schröder W. (1976). Perfect-crystal monochromator for synchrotron x-radiation. J. Appl. Cryst. 9, 223-230.

6. Bos AJJ, Vis RD, Verheul H. (1984). Experimental Comparison of Synchrotron Radiation With Other Modes of Excitation of X-Rays For Trace Element Analysis. Nucl. Instrum. and Meth. 231, April 1984, in press.

7. Bowen DK, Davies ST, Forty AJ. (1983). Microanalytic Studies by Synchrotron Radiation, in: Synchrotron Radiation, Appendix to the Daresbury Annual Report 1982/83, Ref. No. 34, pg. 79.

8. Brown DB, Gilfrich JV, Peckerar MC. (1975). Measurement and Calculation of Absolute Intensities of X-Ray Spectra. J. Appl. Phys. 46, 4537-4540.

9. Cerino J, Stöhr J, Hower N, Bachrach RZ. (1980). An Ultra-High-Vacuum Double Crystal Monochromator Beam Line for Studies in the Spectral Range 500-4000 eV. Nucl. Instrum. and Meth. 172, 227-236.

10. Chen JR, Kneis H, Martin B, Nobiling R, Traxel K, Chao ECT, Minkin JA. (1981). Trace Element Analysis of Bituminous Coals Using the Heidelberg Proton Microprobe. Nucl. Instrum. and Meth. 181, 151-157.

11. Chen JR, Martys N, Chao ECT, Minkin JA, Thompson CL, Hanson AL, Kraner HW, Jones KW. (1984). Synchrotron Radiation Determination of Elemental Concentrations in Coal. Nucl. Instrum. and Meth. 231, April 1984, in press.

12. Codling K. (1973). Applications of Synchrotron Radiation. Rep. Prog. Phys. 36, 541-624.

13. Cramer SP, Dawson JH, Hodgson KO, Hager LP. (1978). Studies on the Ferric Forms of Cytochrome P-450 and Chloroperoxidase by Extended X-Ray Absorption Fine Structure. Characterization of the Fe-N and Fe-S Distances. Am. Chem. Soc. J. 100, 7282-7290.

14. Cramer SP, Eccles TK, Kutzler FW, Hodgson KO, Mortenson LE. (1975). Molybdenum X-Ray Absorption Edge Spectra. The Chemical State of Molybdenum in Nitrogenase. J. Am. Chem. Soc. 98, 1287-1288.

15. Davies ST, Bowen DK, Prins M, Bos AJJ. (1983). Trace Element Analysis by Synchrotron Radiation Excited XRF. Adv. in X-Ray Analysis, 1983, in press.

16. Doniach S, Eisenberger P, Hodgson KO. (1980). X-Ray Absorption Spectroscopy of Biological Molecules, in: Synchrotron Radiation Research, Winick H, Doniach S. (eds.), Plenum Press, NY, 425-458.

17. Eastman DE, Himpsel FJ. (1981). Ultraviolet Radiation - An Incisive and Versatile Tool. Physics Today, May 1981, 64-71.

18. Fletcher NR. (1977). Reevaluation of Background in Superheavy Element Data. Phys. Rev. Lett. 38, 479-481.

19. Fox JD, Courtney WJ, Kemper KW, Lumpkin AH, Fletcher NR, Medsker LR. (1976). Comment on Evidence for Primordial Superheavy Elements. Phys. Rev. Lett. 37, 629-630.

20. Gentry RV, Cahill TA, Fletcher NR, Kaufman HC, Medsker LR, Nelson JW, Flocchini RG. (1976). Evidence for Primordial Superheavy Elements. Phys, Rev. Lett. 37, 11-15.

21. Gilfrich JV, Skelton EF, Nagel DJ, Webb AW. (1983). X-Ray Fluorescence Analysis Using Synchrotron Radiation. Adv. in X-Ray Analysis 26, 313-323.

22. Ginsburg VL, Syrovatskii SI. (1965). Cosmic Magnetobremsstrahlung (Synchrotron Radiation). Ann. Rev. of Astron. and Astrophys. 3, 297-350.

23. Gordon BM. (1983). Uses of Synchrotron Radiation, in: Workshop on Uses of Nuclear Analytical Techniques in Metal Toxicology, Brookhaven National Laboratory, October 11-12, 1982. Neurotoxicology 4, 1983, in press.

24. Gordon BM. (1982). Sensitivity Calculations for Multielemental Trace Analysis by Synchrotron Radiation Induced X-Ray Fluorescence. Nucl. Instrum. and Meth. 204, 223-229.

25. Goulding FS, Jaklevic JM. (1977). XRF Analysis: Some Sensitivity Comparisons Between Charged-Particle and Photon Excitation. Nucl. Instrum. and Meth. 142, 323-332.

26. Goulon J, Lemonnier M, Cortes R, Retournard A, Raoux D. (1983). Development of a New Energy Scanned (4-20 keV) EXAFS-II. Nucl. Instrum. and Meth. 208, 625-630.

27. Greaves GN, Fontaine A, Lagarde P, Raoux D, Gurman SJ. (1981). Local structure of silicate glasses. Nature 293, 611-616.

28. Grodzins L. (1983). Electron, Proton and Photon Induced X-Ray Microprobes: Analytic Sensitivity Versus Spatial Resolution, in: Workshop on Uses of Nuclear Analytical Techniques in Metal Toxicology, Brookhaven National Laboratory, October 11-12, 1982. Neurotoxicology 4, 1983, in press.

29. Hanson AL, Jones KW, Kraner HW, Gordon BM, Chen JR. (1983). The Utilization of Synchrotron Radiation for Trace Element Analyses in Toxicology of Metals, in: Chemical Toxicology and Clinical Chemistry of Metals, Brown SS, Savory J. (eds.), Academic Press, London, 45-48.

30. Hanson AL, Kraner HW, Jones KW, Gordon BM, Mills RE, Chen JR. (1983). Trace Element Measurements with Synchrotron Radiation. IEEE Trans. Nucl. Sci. NS-30, 1339-1342.

31. Harris LA, Barrett HE, Koop C. (1981). Elemental Concentrations and Their Distribution in Two Bituminous Coals of Different Paleoenvironments. Intl. J. Coal Geol. 1, 175-193.

32. Hart M, Rodriques ARD. (1978). Harmonic-free single crystal monochromators for neutron and x-rays. J. Appl. Cryst. 11, 248-253.

33. Horowitz P, Howell JA. (1972). A Scanning X-Ray Microscope Using Synchrotron Radiation. Science 178, 608-611.

34. Howells MR, Hastings JB. (1983). Design Considerations for an X-Ray Microprobe. Nucl. Instrum. and Meth. 208, 379-386.

35. Il'in VE, Kazakevich GM, Kulipanov GN, Mazalov LN, Matyushin AM, Skrinski AN, Sheromov MA. (1977). X-Ray Fluorescence Element Analysis with the Use of Synchrotron Radiation. The Institute of Nuclear Physics, SOAN, USSR, Reprint IYAF 77-57.

36. Jackson JD. (1975). Classical Electrodynamics, 2nd ed., John Wiley and Son, NY, 654-700.

37. Jaklevic J, Kirby JA, Klein MP, Robertson AS, Brown GS, Eisenberger P. (1977). Fluorescence Detection EXAFS: Sensitivity Enhancement for Dilute Species and Thin Films. Solid State Communications 23, 679-682.

38. Jaklevic J, Kirby JA, Ramponi AJ, Thompson AC. (1980). Chemical Characterization of Air Particulate Samples Using X-Ray Absorption Spectroscopy. Environ. Sci. and Tech. 14, 437-441.

39. Jaklevic JM, Walter RL. (1977). Comparison of Minimum Detectable Limits Among X-Ray Spectrometers, in: X-Ray Fluorescence Analysis of Environmental Samples, Dzubay TG (ed.), Ann Arbor Science Inc., Ann Arbor, MI, 63-75.

40. Jones KW, Gordon BM, Hanson AL, Hastings JB, Howells MR, Kraner HW, Chen JR. (1984). Application of Synchrotron Radiation to Elemental Analysis. Nucl. Instrum. and Meth. 231, April 1984, in press.

41. Jordan RG, Jones DW, Durham PJ, Greaves GN, Inglesfield JE. (1983). Near edge X-ray absorption spectra of transition metals, in: Synchrotron Radiation, Appendix to the Daresbury Annual Report 1982/83, Ref. No. 58, pg. 106, Science and Engineering Research Council, Daresbury Laboratory, Warrington, WA4 4AD, U.K.

42. Knöchel A, Petersen W, Tolhiehn G. (1983). X-ray Fluorescence Analysis with Synchrotron Radiation. Nucl. Instrum. and Meth. 208, 659-663.

43. Krinsky S, Thomlinson W, van Steenbergen A. (1982). An Overview of Undulators and Wigglers for the NSLS. BNL Report 31989, NSLS, Brookhaven National Laboratory, Sept. 1982, 1-56.

44. Kunz C (ed.). (1979). Synchrotron Radiation, Springer-Verlag, New York, 1-442.

45. Lee PA, Beni G. (1979). New method for the calculation of atomic phase shifts: Application to extended x-ray absorption fine structure (EXAFS) in molecules and crystals. Phys. Rev. B15, 2862-2883.

46. Lee PA, Pendry JB. (1975). Theory of the extended x-ray absorption fine structure. Phys. Rev. B11, 2795-2811.

47. Lemonnier M, Collet O, Depautex C, Esteva JM, Raoux D. (1978). High Vacuum Two Crystal Soft X-Ray Monochromator. Nucl. Instrum. and Meth. 152, 109-111.

48. Materlik G, Kostroun VO. (1980). Monolithic crystal monochromators for synchrotron radiation with order sorting and polarizing properties. Rev. Sci. Instrum. 51, 86-94.

49. Maylotte DH, Wong J, St. Peters RL, Lytle FW, Greegor RB. (1981). X-Ray Absorption Spectroscopic Investigation of Trace Vanadium Sites in Coal. Science 214, 554-556.

50. McKay GA, Seymour RS. (1982). Electron microprobe analysis of trace elements in minerals at 10 ppm concentrations, in: Microbeam Analysis 1982, Heinrich KFJ (ed.), San Francisco Press, CA, 431-434.

51. Mills D, Pollock V. (1980). Stabilizing feedback system for synchrotron radiation monochromators. Rev. Sci. Instrum. 51, 1664-1668.

52. Minkin JA, Chao ECT, Thompson CL, Nobiling R, Blank H. (1983). Proton Microprobe Determination of Elemental Concentrations in Coal Macerals. Scanning Electron Microsc. 1982; I: 173-184.

53. Minkin JA, Chao ECT, Thompson CL, Wandless MY, Dulong FT, Larson RR, Neuzil SG. (1983). Submicroscopic (<1 μm) Mineral Contents of Vitrinites in Selected Bituminous Coal Beds. Microbeam Analysis, 1983, in press.

54. Munro IH, Sabersky AP. (1980). Synchrotron Radiation as a Modulated Source for Fluorescence Lifetime Measurements and for Time-Resolved Spectroscopy, in: Synchrotron Radiation Research, Winick H, Doniach S (eds.), Plenum Press, NY, 323-352.

55. Pettifer RF, McMillan PW. (1977). Phase-shift calculations for extended X-ray Absorption fine structure (EXAFS) and the fine structure of $As_2O_3$. Philos. Mag. 35, 871-882.

56. Phillips JC, Wlodawer A, Yevitz MM, Hodgson KO. (1976). Applications of Synchrotron Radiation to Protein Crystallography: Preliminary Results. Proc. Nat. Acad. Sci. 73, 128-132.

57. Phizakerly RP, Rek ZU, Stephenson GB, Conradson SD, Hodgson KO, Matsushita T, Oyangi H. (1983). An energy-dispersive spectrometer for the rapid measurement of X-ray absorption spectra using synchrotron radiation. J. Appl. Crystallogr. 16, 220-232.

58. Prins M, Kuiper JM, Viegers MPA. (1984). The design of an x-ray microprobe at the SRS Daresbury (UK). Nucl. Instrum. and Meth. 231, April 1984, in press.

59. Prins M, van der Heide JA, Bos AJ, Bowen K, Davies S. (1983). Trace Element Mapping of Biological Tissues Using PIXE and XRF. IEEE Trans. Nucl. Sci. 30, 1243-1245.

60. Reed SJB. (1975). Electron Microprobe Analysis, Cambridge University Press, Cambridge, England, 1-400.

61. Sayers DE, Heald SM, Pick MA, Budnick JI, Stern EA, Wong J. (1983). X-Ray Beam Line at the NSLS for X-Ray Absorption Studies in Material Sciences. Nucl. Instrum. and Meth. 208, 631-635.

62. Sayers D, Lytle FW, Stern E. (1970). Point Scattering Theory of X-Ray K-Absorption Fine Structure. Adv. in X-Ray Anal. 13, 248-271.

63. Schwinger J. (1949). On the Classical Radiation of Accelerated Electrons. Phys. Rev. 75, 1912-1925.

64. Shulman RG, Eisenberger P, Teo BK, Kincaid BM, Brown GS. (1978). Fluorescence X-Ray Absorption Studies of Rubredoxin and Its Model Compounds. J. Mol. Biol. 124, 305-321.

65. Solid State Sciences Committee, National Academy of Sciences. (1983). Current Status of Facilities Dedicated to the Production of Synchrotron Radiation. National Academy of Science, 2101 Constitution Ave., Washington, DC, 1-40.

66. Sparks Jr, CJ. (1980). X-Ray Fluorescence Microprobe For Chemical Analysis, in: Synchrotron Radiation Research, Winick H, Doniach S (eds.), Plenum Press, NY, 459-512.

67. Sparks Jr, CJ, Raman S, Ricci E, Gentry RV, Krause MO. (1979). Evidence Against Superheavy Elements in Giant-Halo Inclusions Re-examined with Synchrotron Radiation. Phys. Rev. Lett. 40, 507-511.

68. Sparks Jr, CJ, Raman S, Yakel HL, Gentry RV, Krause MO. (1977). Search with Synchrotron Radiation for Superheavy Elements in Giant-Halo Inclusions. Phys. Rev. Lett. 38, 205-208; Errata: Phys. Rev. Lett. 38, 205 (1977).

69. Stern EA, Heald SM. (1979). X-ray filter assembly for fluorescence measurements of x-ray absorption fine structure. Rev. Sci. Instrum. 50, 1579-1582.

70. van Steenbergen A, NSLS Staff. (1980). The National Synchrotron Light Source Basic Design and Project Status. Nucl. Instrum. and Meth. 172, 25-32.

71. Watson RE. (1983). An Overview of United States Synchrotron Radiation Facilities. Third National Conference on Synchrotron Radiation Instrumentation, Sept. 12-14, Brookhaven National Laboratory, Upton, NY. Nucl. Instrum. and Meth., in press.

72. Williams GP, Thomson RE. (1983). Flux Output from the NSLS X-Ray Ring Dipoles at 1.2-2.5 GeV from 0.6 Å to 100 Å. BNL report 32580, National Synchrotron Light Source, Brookhaven National Laboratory, Upton, NY.

73. Winick H, Doniach S (eds.). (1980). Synchrotron Radiation Research, Plenum Press, NY, 1-754.

74. Wong J. (1981). EXAFS studies of local structure and dynamics in glassy solids. J. Non-cryst. Solids 40, 625.

75. Wuilleumier FJ. (1981). Atomic Physics with Synchrotron Radiation, in: Proc. of the 7th Intl. Conf. on Atomic Phys., Atomic Phys. 7, Kleppner D, Pipkin FM (eds.), Plenum Press, NY, 491-527.

76. Zubovic P. (1976). Geochemistry of Trace Elements in Coal, in: Ayer FA, compiler, Environmental Aspects of Fuel Conversion Technology II, US EPA, Environ. Protection. Tech. Ser. EPA-600/2-76-149, 47-63.

## Discussion with Reviewers

A.J.J. Bos: What is the maximum theoretical reduction of the background Rayleigh and Compton scattering due to the polarization of the incident synchrotron radiation?
*Authors:* Equations (12) and (13) in the text indicate that the background counts are minimized with the x-ray detector at $\theta = 90°$ and in the $(\epsilon_{o//}, k_o)$ plane. The reduction factor is on the order of $10^3$, but is highly dependent on experimental parameters such as the energy of the synchrotron radiation beam and the target thickness which determine, for example, the amount of multiple scattering; figure 2 of reference 18 gives a plot of background reduction versus energy.

A.J.J. Bos: From the given increased cross sections and reduced background in SXRF, 10-$10^3$ lower limits of detection are expected. However, the results of reference 30 and reference 6 show only evidence for not more than a factor of 6.
*Authors:* The theoretical lower limits of detection are based on 1) 100% linearly polarized synchrotron radiation and 2) an x-ray detector located exactly at $\theta = 90°$ and in the electron orbital plane. As we indicate in the text, the synchrotron radiation beam is only fully polarized in the electron orbital plane; with increasing azimuthal angle (out of the electron orbital plane), the polarization changes from linear to elliptical. This decreased linear polarization must be taken into account since, in practice, an x-ray detector such as a Si(Li) or Ge(Li) detector subtends a "large" solid angle. In addition the background Compton cross section is a sensitive function of $\theta$; the finite solid angle of the x-ray detector will cause an increase

in the background Compton counts due to the range of values of θ accepted. The overall gain of SXRF using solid state detectors over conventional XRF is therefore on the order of 10. See also reference 42. With a wavelength dispersive spectrometer the smaller solid angle subtended and the greater energy resolution will allow reduction in the limits of detection approaching $10\text{-}10^3$. See also reference 28.

S. Csillag: You are stating that the radiation damage produced by the synchrotron radiation in the sample is $10^3$ - $10^5$ times less compared with other technics (protons or electrons). This is certainly true when heavier elements are being studied. For low Z elements however (first and second row in the periodic table) the X-ray yield is rather small. This coupled with the fact that the detector is subtending a very small solid angle at the specimen yields a rather low detection efficiency per incident X-ray. Whereas in EELS for instance where basically every event can be detected (since the inelastically scattered electrons are sharply forward peaked) and parallel detection system can be implemented the detection efficiency can be $10^3$ - $10^4$ higher over the system described in this work. This allows rather small doses to be used and consequently the radiation damage can be reduced to the same level or even below the damage level produced by X-rays.

Authors: The use of x-rays over electrons and protons becomes less advantageous under experimental conditions requiring a) thin targets (discussed in the text under x-ray fluorescence microprobes) or b) the study of low Z elements with small x-ray cross sections, as you indicate. A higher incident x-ray flux can be used to compensate for the lower target profile in a) and b) above, however the radiation damage will increase correspondingly.

The SXRF method is in general not used as a surface technique or for the study of low Z elements, in which case the above situations in a) and b) above are not obtained.

S. Csillag: When comparing the MDL's achievable with electron microprobes and synchrotron X-ray fluorescence microprobes the MDL's mentioned in this work ($10^{-6}$ - $10^{-9}$ g/cm$^2$) were obtained from spots with several microns in diameter whereas using electron microprobes one can obtain 10-100 ppm from spots which are $\sim 10^6$ smaller than the one mentioned in this work.

This means that if you have a uniform elemental concentration of the element to be studied over large areas of the sample the MDL obtainable with synchrotron X-rays microprobe is lower. However, if the element to be studied is concentrated into small clusters in the sample (and this is the case in many practical situations in materials science and biology) the electron microprobes will perform much better than X-rays.

Authors: For samples that are thin compared to the interaction volume, electron beam spreading is approximately equal to the sample thickness. Thus one is restricted to very thin samples with electron microprobes in order to keep the electron beam from creating large interaction volumes.

For thick samples, even though much smaller electron beam spots can be achieved, the electron beam is scattered in the sample which typically produces a 1 μm diameter source of x-rays. For example, a Newbury and Yakowitz show that a 20 keV electron beam will produce an interaction volume of ≈2 μm diameter in Al, ≈1 μm diameter in Cu, and ≈0.4 μm diameter in Au (Newbury DE, Yakowitz H. (1976). in: Use of Monte Carlo Calculations in Electron Probe Microanalysis and Scanning Electron Microscopy, Heinrich KFJ, Newbury DE, Yakowitz H (eds.), Natl Bur. Stand. U.S. Spec. Publ. 460, 15-44). Thus a spatial resolution of about 1 μm for an x-ray microprobe is competitive with that obtained in electron microprobes for thick samples.

A.J.J. Bos: What is the thickness of the (NBS-reference materials) target used by Sparks (ref. 66)? The better limit of detection found by Sparks (55 ± 10 times) is based on a not so far detected superheavy element. What does it yield for an existing element?

Authors: The NBS reference materials used and their thicknesses were as follows: orchard leaves (SRM 1571) 178 mg/cm$^2$, bovine liver (SRM 1577) 100 mg/cm$^2$, and coal (SRM 1632) 85 mg/cm$^2$.

Using a synchrotron radiation beam at 37 keV the MDL for Cd (K-α line) was found to be 0.0003 ng, which is approximately 25 times lower than the MDL found using a PIXE microbeam. Further lowering of the MDL could have been achieved by optimizing the synchrotron beam energy (S. Raman, unpublished data).

S. Csillag: In implementing the energy dispersion EXAFS technique how are you going to measure $I_o$? Also how high energy resolution can you obtain from a curved crystal the type you are mentioning?

Authors: For most measurements the event rate can be normalized to the output of an ionization chamber placed in the incident synchrotron radiation beam. In addition, $I_o$ can be calculated from the detector efficiency and a known standard target.

The energy resolution depends on 1) the characteristics of the incident beam and 2) the spatial resolution of the position sensitive detector. An energy resolution of 5 eV for energy dispersive EXAFS using a curved Ge crystal has been reported by Flank et al. (Flank AM, Fontaine A, Jucha A, Lemonnier M, Raoux D, Williams C. (1983). EXAFS in Dispersive Mode. Nucl. Instrum. and Meth. 208, 651-654.) A large improvement in the energy resolution is expected with the smaller source sizes of the new generation of storage rings designed for synchrotron radiation production.

A.J.J. Bos: How is the limit of detection defined?

Authors: The minimum detectable limit (MDL) is given by the expression:

$$MDL = 3.9\ C\sqrt{BG}/N$$

where C is the mass fraction, N is the net number of counts in the peak after background

subtraction and BG is the number of counts in the background. We refer you to Currie LA. (1968). Limits for qualitative detection and quantitative determination. *Anal. Chem.* 40, 586-593.

A.J.J. Bos: What is the absolute limit of detection found by Il'in (ref. 35)?
Authors: Il'in reports MDL's (obtained in 1000s) of $1.6 \times 10^{-8}$ and $7.2 \times 10^{-8}$ $gg^{-1}$ for Zn and Au, respectively, in aqueous solutions.